

# Entropy-based viscous regularization for the multi-dimensional Euler equations in low-Mach regimes

Marc O. Delchini<sup>a</sup>, Jean C. Ragusa<sup>\*,a</sup>, Ray A. Berry<sup>b</sup>

<sup>a</sup>*Department of Nuclear Engineering, Texas A&M University, College Station, TX 77843, USA*

<sup>b</sup>*Idaho National Laboratory, Idaho Falls, ID 83415, USA*

---

## Abstract

The entropy viscosity method, introduced by Guermond et al. [1, 2], is extended to the multi-dimensional Euler equations for both subsonic (very low Mach numbers) and supersonic flows. We show that the current definition of the viscosity coefficients [1] is not adapted to low-Mach flows and we provide a robust alternate definition valid for any Mach number value. The new definitions are derived from a low-Mach asymptotic study. In addition, the entropy minimum principle is used to derive the viscous regularization terms for Euler equations with variable area for nozzle flow problems. Various 1- and 2-D numerical tests are presented : flow in a convergent-divergent nozzle, Leblanc shock tube, subsonic flow around a 2-D cylinder and over a circular hump, and supersonic flow in a compression corner. Convergence studies are performed using analytical solutions in 1-D. Both the ideal gas and stiffened gas equations of state are employed.

*Key words:* Euler equations with variable area, entropy viscosity method, stabilization method, low Mach regime, shocks.

---

## 1. Introduction

Over the past years an increasing interest raised for computational methods that can solve both compressible and incompressible flows. In engineering applications, there is often the need to solve for complex flows where a near incompressible regime or low Mach flow coexists with a supersonic flow domain. For example, such flow are encountered in aerodynamic in the study of airships. In the nuclear industry, flows are nearly the incompressible regime but compressible effects cannot be neglected because of the heat source and thus needs to be accurately resolved. When solving the multi-D Euler equations for a wide range of Mach numbers,

---

<sup>\*</sup>Corresponding author

*Email addresses:* `delchmo@tamu.edu` (Marc O. Delchini), `jean.ragusa@tamu.edu` (Jean C. Ragusa), `ray.berry@inl.gov` (Ray A. Berry)

multiple problems have to address: stability, accuracy and acceleration of the convergence in the low Mach regime. Because of the hyperbolic nature of the equations, shocks can form during transonic and supersonic flows, and require the use of the numerical methods in order to stabilize the scheme and correctly resolve the discontinuities. The literature offers a wide range of stabilization methods: flux-limiter [3, 4], pressure-based viscosity method ([5]), Lapidus method ([6, 7, 8]), and the entropy-viscosity method([1, 2]) among others. These numerical methods are usually developed using simple equation of states and tested for transonic and supersonic flows where the disparity between the acoustic waves and the fluid speed is not large since the Mach number is of order one. This approach leads to a well-known accuracy problem in the low Mach regime where the fluid velocity is smaller than the speed of sound by multiple order of magnitude. The numerical dissipative terms become ill-scaled in the low Mach regime and lead to the wrong numerical solution by changing the nature of the equations solved. This behavior is well documented in the literature [9, 10, 11] and often treated by performing a low Mach asymptotic study of the multi-D Euler equation. This method was originally used [9] to show convergence of the compressible multi-D Euler equations to the incompressible ones. Thus, by using the same method, the effect of the dissipative terms in the low Mach regime, can be understood and, when needed, a fix is developed in order to ensure the convergence of the equations to the correct physical solution. This approach was used as a fixing method for multiple well known stabilization methods alike Roe scheme ([12]) and SUPG [11] while preserving the original stabilization properties of shocks.

We propose, through this paper, to investigate how the entropy viscosity method, when applied to the multi-D Euler equations with variable area, behaves in the low Mach regime. This method was initially introduced by Guermond et al. to solve for the hyperbolic systems and has shown good results when used for solving the multi-D Euler equations with various discretization schemes. More importantly, it is simple to implement, can be used with unstructured grids, and its dissipative terms are consistent with the entropy minimum principle and proven valid for any equation of state under certain conditions [13].

This paper is organized as follows: in Section 2 the current definition of the entropy viscosity method is recalled, and inconsistency with the low Mach regime are pointed out. Since our interest is in the variable area version of the multi-D Euler equation, the reader is guided through the steps leading to the derivation of the dissipative terms on the model of [13]. Then in Section 3, a new definition of the viscosity coefficient is introduced and derived from a low Mach asymptotic study. After detailing the spatial and temporal discretization method in Section 4, 1- and 2-D numerical results are presented in Section 5 for a wide range of Mach numbers: low Mach flow over a cylinder and a circular bump, and supersonic flow in a compression corner [14]. Convergence studies are performed in 1-D, in order to demonstrate the accuracy of the solution.

For purpose of clarity, the multi-D Euler equations with variable area are re-

55 called in Eq. (1) and the corresponding variables are defined:

$$\begin{cases} \partial_t (\rho A) + \vec{\nabla} \cdot (\rho \vec{u} A) = 0 \\ \partial_t (\rho \vec{u} A) + \vec{\nabla} \cdot [(\rho \vec{u} \otimes \vec{u} + P \mathbf{I}) A] = P \vec{\nabla} A \\ \partial_t (\rho E A) + \vec{\nabla} \cdot [\vec{u} (\rho E + P) A] = 0 \\ P = P(\rho, e) \end{cases} \quad (1)$$

56 where  $\rho$ ,  $\rho \vec{u}$  and  $\rho E$  are the density, the momentum and the total energy, re-  
 57 spectively, and will be referred to as the conservative variables. The pressure  
 58  $P$  is computed with an equation of state expressed in function of the density  $\rho$   
 59 and the specific internal energy  $e$ . The tensor product  $\vec{a} \otimes \vec{b}$  is taken with the  
 60 following convention:  $(\vec{a} \otimes \vec{b})_{i,j} = a_i b_j$ . Lastly, the terms  $\partial_t$ ,  $\vec{\nabla}$ ,  $\vec{\nabla} \cdot$  and  $\mathbf{I}$  denote  
 61 the temporal derivative, the gradient and divergent operators, and the identity  
 62 tensor, respectively. The variable area  $A$  is assumed spatial dependent.

## 63 2. The Entropy Viscosity Method

### 64 2.1. Background

65 In this section, the entropy-based viscosity method [1, 2, 15] is recalled for  
 66 the multi-D Euler equations (with constant area  $A$ ) [16]. The entropy-based  
 67 viscosity method consists of adding dissipative terms, with a viscosity coeffi-  
 68 cient modulated by the entropy production which allows high-order accuracy  
 69 when the solution is smooth. Thus, two questions arise: (i) how are the viscos-  
 70 ity dissipative terms derived and (ii) how to numerically compute the entropy  
 71 production. Answers to the first question can be found in [13] by Guermond et  
 72 al., that details the proof leading to the derivation of the artificial dissipative  
 73 terms (Eq. (2)) consistent with the entropy minimum principle theorem. The  
 74 viscous regularization obtained is valid for any equation of state as long as the  
 75 opposite of the physical entropy function,  $s$ , is convex with respect to the in-  
 76 ternal energy  $e$  and the specific volume  $1/\rho$ . As for the entropy production, it  
 77 is locally evaluated by computing the local entropy residual  $D_e(\vec{x}, t)$  defined in  
 78 Eq. (4), that is known to be peaked in shocks [17].

$$\begin{cases} \partial_t (\rho) + \vec{\nabla} \cdot (\rho \vec{u}) = \vec{\nabla} \cdot (\kappa \vec{\nabla} \rho) \\ \partial_t (\rho \vec{u}) + \vec{\nabla} \cdot (\rho \vec{u} \otimes \vec{u} + P \mathbf{I}) = \vec{\nabla} \cdot (\mu \rho \vec{\nabla}^s \vec{u} + \kappa \vec{u} \otimes \vec{\nabla} \rho) \\ \partial_t (\rho E) + \vec{\nabla} \cdot [\vec{u} (\rho E + P)] = \vec{\nabla} \cdot (\kappa \vec{\nabla} (\rho e) + \frac{1}{2} \|\vec{u}\|^2 \kappa \vec{\nabla} \rho + \rho \mu \vec{u} \vec{\nabla} \vec{u}) \\ P = P(\rho, e) \end{cases} \quad (2)$$

79 where  $\kappa$  and  $\mu$  are local positive viscosity coefficients.  $\vec{\nabla}^s \vec{u}$  denotes the sym-  
 80 metric gradient operator that guarantees the method to be rotational invariant  
 81 [13].

82 In the current version of the method,  $\kappa$  and  $\mu$  are set equal, so that the above  
 83 viscous regularization (Eq. (2)) is equivalent to the parabolic regularization  
 84 [18] when considering the 1-D form of the equation. The current definition in-  
 85 cludes a first-order viscosity coefficient referred to with the subscript *max*, and

a high-order viscosity coefficient referred to with the subscript  $e$ . The first-order viscosity coefficients  $\mu_{max}$  and  $\kappa_{max}$  are proportional to the local largest eigenvalue  $||\vec{u}|| + c$  and equivalent to an upwind-scheme (see Eq. (3)), when used, which is known to be over-dissipative and monotone [17]:

$$\mu_{max}(\vec{r}, t) = \kappa_{max}(\vec{r}, t) = \frac{h}{2} (||\vec{u}|| + c), \quad (3)$$

where  $h$  is defined as the ratio of the grid size to the polynomial order of the test functions used.

The second-order viscosity coefficients  $\kappa_e$  and  $\mu_e$  are set proportional to the entropy production that is evaluated by computing the local entropy residual  $D_e$ . It also includes the interfacial jump of the entropy flux  $J$  that will allow to detect any discontinuities other than shocks:

$$\mu_e(\vec{r}, t) = \kappa_e(\vec{r}, t) = h^2 \frac{\max(|D_e(\vec{r}, t)|, J)}{||s - \bar{s}||_\infty} \text{ with } D_e(\vec{r}, t) = \partial_t s + \vec{u} \cdot \vec{\nabla} s \quad (4)$$

where  $||\cdot||_\infty$  and  $\bar{\cdot}$  denote the infinite norm operator and the average operator over the entire computational domain, respectively. The definition of the jump  $J$  is discretization-dependent and examples of definition can be found in [16] for DGFEM. The denominator  $||s - \bar{s}||_\infty$  is used for dimensionality purposes and should not be of the same order as  $h$ , on penalty of losing the high-order accuracy. Currently, there are no theoretical justification for choosing the denominator.

The definition of the viscosity coefficients  $\mu$  and  $\kappa$  is function of the first- and second-order viscosity coefficients as follows:

$$\mu(\vec{r}, t) = \min(\mu_e(\vec{r}, t), \mu_{max}(\vec{r}, t)) \text{ and } \kappa(\vec{r}, t) = \min(\kappa_e(\vec{r}, t), \kappa_{max}(\vec{r}, t)). \quad (5)$$

This definition allows the following properties. In shock regions, the second-order viscosity coefficient experiences a peak because of entropy production, and thus, saturates to the first-order viscosity that is known to be over-dissipative and will smooth out oscillations. Anywhere else, the entropy production being small, the viscosity coefficients  $\mu$  and  $\kappa$  are of order  $h^2$ .

Using the above definition of the entropy-based viscosity method, high-order accuracy was demonstrated and excellent results were obtained with 1-D Sod shock tubes and various 2-D tests [1, 2, 16].

## 2.2. Issues in the Low-Mach Regime

In the Low-Mach Regime, the flow is known to be isentropic resulting in very little entropy production. Since the entropy viscosity method is directly based on the evaluation of the local entropy production, it will be interested to study how the entropy viscosity coefficients  $\mu$  and  $\kappa$  scale in the low Mach regime. Mathematically, it means that the entropy residual  $D_e$  will be very small, so will be the denominator  $||s - \bar{s}||_\infty$ , thus making the ratio, used in the definition of the viscosity coefficients Eq. (4), undetermined. Therefore, the

current definition of the viscosity coefficients seems unadapted to subsonic flow and could lead to ill-scaled dissipative terms. A solution would be to recast the entropy residual as a function of other variables in order to have more freedom in the choice of the normalization parameter. With this approach, the viscosity coefficients are still defined proportional to the entropy residual that is a good indicator of the flow type (subsonic, transonic and supersonic flow). Plus, a different normalization parameter could be chosen, based on a low Mach asymptotic study so that the viscosity coefficients are well-scaled in the low Mach asymptotic limit (see Section 3).

### 2.3. The dissipative-terms for the multi-D Euler equations with variable area

One of the focus of this paper is to investigate the application of the entropy viscosity method to the multi-D Euler equations with variable area. The variable area version of the Euler equations is mostly used in 1-D and 2-D for obvious reasons, and differs from Eq. (1) by the momentum equation as shown in Eq. (6), that contains a non-conservative term proportional to the area gradient. For the purpose of this paper, the variable area is assumed to be a smooth function and only spatial dependent. An example can be found in [19] where a fluid flows through a 1-D convergent-divergent nozzle and reaches a steady-state solution.

$$\begin{cases} \partial_t (\rho A) + \vec{\nabla} \cdot (\rho \vec{u} A) = 0 \\ \partial_t (\rho \vec{u} A) + \vec{\nabla} \cdot [A (\rho \vec{u} \otimes \vec{u} + P \mathbf{I})] = P \vec{\nabla} A \\ \partial_t (\rho E) + \vec{\nabla} \cdot [\vec{u} (\rho E + P)] = 0 \end{cases} \quad (6)$$

The application of the entropy viscosity method to the above system of equations is expected to be straightforward since it degenerates to the Eq. (1) when assuming a constant area. Details of the derivations of the dissipative terms are available to the reader in Appendix B and are very similar to what was done in [13]. An entropy residual is derived without the dissipative terms. Then, the same entropy residual is re-derived after adding dissipative terms to each equation of the system given in Eq. (6), and the entropy minimum principle is used as a condition to obtain a definition for each of the dissipative terms. The final result including the dissipative terms is given in Eq. (7):

$$\begin{cases} \partial_t (\rho A) + \vec{\nabla} \cdot (\rho \vec{u} A) = \vec{\nabla} \cdot (A \kappa \vec{\nabla} \rho) \\ \partial_t (\rho \vec{u} A) + \vec{\nabla} \cdot [A (\rho \vec{u} \otimes \vec{u} + P \mathbf{I})] = P \vec{\nabla} A + \vec{\nabla} \cdot \left[ A \left( \mu \rho \vec{\nabla}^s \vec{u} + \kappa \vec{u} \otimes \vec{\nabla} \rho \right) \right] \\ \partial_t (\rho E) + \vec{\nabla} \cdot [\vec{u} (\rho E + P)] = \vec{\nabla} \cdot \left[ A \left( \kappa \vec{\nabla} (\rho e) + \frac{1}{2} \|\vec{u}\|^2 \kappa \vec{\nabla} \rho + \rho \mu \vec{u} \vec{\nabla} \vec{u} \right) \right] \end{cases} \quad (7)$$

The dissipative terms are very similar to the ones obtained for the multi-D Euler equations: each dissipative flux is multiplied by the variable area  $A$  in order to ensure conservation of the flux. When assuming a constant area, Eq. (2) is retrieved. The definition of the viscosity coefficients  $\mu$  and  $\kappa$  is explained in Section 3.2.

### 153 3. All-speed Reformulation of the Entropy Viscosity Method

154 In this section, the entropy residual  $D_e$  is recast as a function of the pressure,  
155 the density and the speed of sound. Then, a low Mach asymptotic study of the  
156 multi-D Euler equations is performed in order to derive the correct normalization  
157 parameter.

#### 158 3.1. New Entropy Production Residual

159 The first step in defining a viscosity coefficient that behaves well in the low  
160 mach limit is to recast the entropy residual in terms of the thermodynamic  
161 variables as shown in Eq. (8):

$$D_e(\vec{r}, t) = \partial_t s + \vec{u} \cdot \vec{\nabla} s = \frac{s_e}{P_e} \left( \underbrace{\frac{dP}{dt} - c^2 \frac{d\rho}{dt}}_{\tilde{D}_e(\vec{r}, t)} \right), \quad (8)$$

162 where  $\frac{d}{dt}$  denotes the material or total derivative, and  $P_e$  is the partial derivative  
163 of pressure with respect to internal energy. The steps that lead to the new  
164 formulation of the entropy residual  $D_e$  can be found in Appendix A.

165 The entropy residual  $D_e$  and  $\tilde{D}_e$  are proportional to each other and therefore  
166 will experience the same variation when taking the absolute value. Thus, locally  
167 evaluating  $\tilde{D}_e$  instead of  $D_e$  should allow us to measure the entropy production  
168 point wise. This new expression given in Eq. (8) has multiple advantages:

- 169 • an analytical expression of the entropy function is not longer needed: the  
170 entropy residual  $\tilde{D}_e$  is evaluated using the local values of the pressure, the  
171 density and the speed of sound. Deriving an entropy function for some  
172 complex equation of states can be difficult.
- 173 • with the proposed expression of the entropy residual function of pressure  
174 and density, additional normalizations suitable for low Mach flows of the  
175 entropy residual can be devised. Examples include the pressure itself,  
176 or combination of the density, the speed of sound and the norm of the  
177 velocity:  $\rho c^2$ ,  $\rho c ||\vec{u}||$  and  $\rho ||\vec{u}||^2$ .

178 The viscosity coefficients  $\mu$  and  $\kappa$  are now defined proportional to the new  
179 entropy residual  $\tilde{D}_e$  on the model of Eq. (4) as follows:

$$\mu(\vec{r}, t) = \kappa(\vec{r}, t) = h^2 \frac{\max(\tilde{D}_e, J)}{n(P)} \quad (9)$$

180 where  $n(P)$  is a normalization parameter to determine and all other variables  
181 were defined previously.

182 As mentioned earlier, the normalization parameter  $n(P)$  must be of the same  
183 units as the pressure for the viscosity coefficients to have the unit of a dy-  
184 namic viscosity ( $m^2/s$ ). Multiples options are available to us:  $P$ ,  $\rho c^2$ ,  $\rho c ||\vec{u}||$

185 and  $\rho||\vec{u}||^2$ . The choice of the normalization parameter cannot be random if  
 186 the definition of the viscosity coefficient is wanted to be well-scaled for a wide  
 187 range of Mach numbers. For example, by choosing  $n(P) = \rho||\vec{u}||^2$ , the viscosity  
 188 coefficient will become very large as the Mach number decreases which would  
 189 be unnecessary since the equations will not develop any shock or discontinuity.  
 190 Therefore, it is proposed to carry, in Section 3.2, a low-Mach asymptotic study  
 191 of the multi-D Euler equations in order to determine the correct expression for  
 192 the normalization parameter  $n(P)$ .

### 193 3.2. Low-Mach asymptotic study of the multi-D Euler equations

194 The asymptotic study requires the multi-D Euler equations to be non di-  
 195 mensionalized: the objective is to make the Mach number appears and thus,  
 196 use a polynomial expansion of the variables as a function of the Mach number  
 197 in order to derive the leading, first- and second-order equations. Before detailing  
 198 the steps of the asymptotic method, let us have a closer look at the system of  
 199 equations under consideration. The initial system of equations is composed of  
 200 the multi-D Euler equations. For stability purpose, artificial dissipative terms  
 201 are added to each equation as explained in Section 2. The resulting system of  
 202 equations is alike the multi-D Navier-Stokes equations in a sense that it con-  
 203 tains second-order derivative terms. Thus, it would be interesting to look at the  
 204 steps employed in the asymptotic study of the multi-D Navier-Stokes equations  
 205 in order to understand how the dissipative terms are treated. Fortunately, this  
 206 process is well-documented in the literature [9, 10, 11] for both multi-D Euler  
 207 equations and Navier-Stokes equations. The work presented here is mainly in-  
 208 spired of [20] that focuses on the asymptotic study in the low Mach regime of  
 209 Navier-Stokes equations. During the derivation, the reader has to keep in mind  
 210 that the objective of this section is to derive the scaling of the normalization  
 211 parameter  $n(P)$  involved in the definition of the viscosity coefficients given in  
 212 Eq. (4), so that the multi-D Euler equations degenerate to the incompressible  
 213 system of equations, which implies that the dissipative terms are well-scaled.  
 214 The main steps of the derivation are presented in the following of this section.  
 215 To express Eq. (2) in dimensionless variables, the following dimensional variables  
 216 are introduced:

$$\begin{aligned} \rho &= \frac{\rho^*}{\rho_\infty}, P = \frac{P^*}{\rho_\infty c_\infty^2}, \mu = \frac{\mu^*}{\mu_\infty}, E = \frac{E^*}{c_\infty^2}, \mu = \frac{\mu^*}{\mu_\infty}, \\ \kappa &= \frac{\kappa^*}{\kappa_\infty}, x = \frac{x^*}{L_\infty}, t = \frac{t^*}{L_\infty/u_\infty}, u = \frac{u^*}{u_\infty} \end{aligned} \quad (10)$$

217 where the subscript  $\infty$  and the upper script  $*$  denote the far field or stagnation  
 218 quantities and the dimensionless variables, respectively. The reference quantities  
 219 are chosen such that the non dimensional flow quantities are of order one for  
 220 any low reference-Mach number

$$M_\infty = \frac{u_\infty^*}{c_\infty^*} \quad (11)$$

where  $c_\infty^*$  is a reference value for the speed of sound.  
 Then, using the non dimensional quantities and the multi-D Euler equations  
 from Eq. (2) , the following non dimensional form is obtained:

$$\begin{cases} \partial_t \rho + \nabla \cdot (\rho \vec{u}) = \frac{1}{Re_\infty Pr_\infty} \nabla \cdot (\kappa \nabla \rho) \\ \partial_t (\rho \vec{u}) + \nabla \cdot (\rho \vec{u} \otimes \vec{u}) + \frac{1}{M_\infty^2} \nabla (P) = \frac{1}{Re_\infty} \nabla (\rho \mu \nabla \vec{u}) + \frac{1}{Re_\infty Pr_\infty} \nabla \cdot (\vec{u} \otimes \kappa \nabla \rho) \\ \partial_t (\rho E) + \nabla \cdot [\vec{u} (\rho E + P)] = \frac{1}{Re_\infty Pr_\infty} \nabla \cdot (\kappa \nabla (\rho e)) + \frac{M_\infty^2}{Re_\infty} \nabla \cdot (\vec{u} \rho \mu \nabla \vec{u}) \\ + \frac{M_\infty^2}{2 Re_\infty Pr_\infty} \nabla \cdot (\kappa u^2 \nabla \rho) \\ P = (\gamma - 1) (\rho E + M_\infty^2 \rho u^2) \end{cases} \quad (12)$$

where the *numerical* Reynolds ( $Re_\infty$ ) and Prandtl ( $Pr_\infty$ ) numbers are defined  
 as follows:

$$Re_\infty = \frac{u_\infty L_\infty}{\mu_\infty} \text{ and } Pr_\infty = \frac{\mu_\infty}{\kappa_\infty}. \quad (13)$$

Once the dimensionless equations are obtained, the next step consists of expanding  
 each variable in term of the Mach number (example given in Eq. (14) for  
 the pressure  $P$ ) in order to derive the leading, first- and second-order equations.

$$P(\vec{r}, t) = P_0(\vec{r}, t) + P_1(\vec{r}, t) M_\infty + P_2(\vec{r}, t) M_\infty^2 + \dots \text{ with } M_\infty \rightarrow 0 \quad (14)$$

From Eq. (15), it is observed that the scaling of the Reynolds and Prandtl  
 numbers will affect the asymptotic equations because of the dissipative terms.  
 By studying the effect of the dissipative terms onto the asymptotic equations,  
 the scaling of the viscosity coefficients  $\mu$  and  $\kappa$  can be determined so that the  
 pressure and velocity fluctuations remain of the order of the Mach number  
 square and the Mach number, respectively. For the purpose of this section it is  
 assumed that the Reynolds and Prandtl numbers scale as the Mach number to  
 the power  $n$  and  $m$ , respectively:  $Re_\infty = M_\infty^n$  and  $Pr_\infty = M_\infty^m$  with  $\{n, m\} \in \mathbb{Z}^2$ .  
 Different values for the pair  $\{n, m\}$  are investigated. It is also noted that  
 having  $n = m$  is equivalent to setting the viscosity coefficients  $\mu$  and  $\kappa$  equal.  
 The objective of this investigation is to make a choice on the scaling of the  
 Reynolds and Prandtl numbers, obtain the corresponding asymptotic equations,  
 and determine whether or not the low Mach asymptotic limit is preserved. Since  
 the Reynolds and Prandtl numbers are function of the viscosity coefficients and  
 thus, of the normalization parameter  $n(P)$  defined in Eq. (10), a scaling for the  
 function  $n(P)$  will be derived as well.

- $Re_\infty = Pr_\infty = 1$  or  $m = n = 0$ :  
 Using the assumption  $m = n = 0$ , the system of equation given in Eq. (15)



247

becomes:

$$\left\{ \begin{array}{l} \partial_t \rho + \nabla \cdot (\rho \vec{u}) \\ \partial_t (\rho \vec{u}) + \nabla \cdot (\rho \vec{u} \otimes \vec{u}) + \frac{1}{M_\infty^2} \nabla \cdot (P) \\ \partial_t (\rho E) + \nabla \cdot [\vec{u} (\rho E + P)] \\ + M_\infty^2 \nabla \cdot (\kappa u^2 \nabla \rho) \\ P = (\gamma - 1) (\rho E + M_\infty^2 \rho u^2) \end{array} \right. = \begin{array}{l} \nabla \cdot (\kappa \nabla \rho) \\ \nabla \cdot (\rho \mu \nabla^s \vec{u}) + \nabla \cdot (\vec{u} \otimes \kappa \nabla \rho) \\ \nabla \cdot (\kappa \nabla (\rho e)) + M_\infty^2 \nabla \cdot (\vec{u} \rho \mu \nabla^s \vec{u}) \end{array} \quad (15)$$

248

The following asymptotic equations are obtained:

At order  $M_\infty^{-2}$ :

$$\vec{\nabla} P_0 = 0$$

At order  $M_\infty^{-1}$ :

$$\vec{\nabla} P_1 = 0$$

At order 1:

$$\begin{aligned} \partial_t \rho_0 + \vec{\nabla} \cdot (\rho_0 \vec{u}_0) &= \vec{\nabla} \cdot (\kappa_0 \vec{\nabla} \rho_0) \\ \partial_t (\rho_0 \vec{u}_0) + \vec{\nabla} \cdot (\rho_0 \vec{u}_0 \otimes \vec{u}_0) + \vec{\nabla} P_2 &= \vec{\nabla} \cdot (\rho_0 \mu_0 \vec{\nabla}^s \vec{u}_0 + \kappa_0 \vec{u}_0 \otimes \vec{\nabla} \rho_0) \\ \partial_t (\rho_0 E_0) + \vec{\nabla} \cdot [\vec{u}_0 (\rho_0 E_0 + P_0)] &= \vec{\nabla} \cdot (\kappa_0 \vec{\nabla} (\rho_0 e_0)) \end{aligned}$$

249

250

251

252

253

254

255

256

From the first two asymptotic equations, it is concluded that the leading- and first-order pressure are constant in space. Thus, the pressure fluctuation will be of order to the Mach number square as required:  $P(\vec{x}, t) = P_0(t) + M_\infty^2 \cdot P_2(\vec{x}, t)$  where  $P_1$  subsumed in  $P_0$ . It remains to investigate how the velocity fluctuations scale as a function of the Mach number. Using the equation of state to relate the leading-order pressure to the total and internal energy, the first-order energy equation can be recast as follows:

$$(\gamma - 1) \partial_t P_0 + \gamma \vec{\nabla} \cdot (\vec{u}_0 P_0) = (\gamma - 1) \vec{\nabla} \cdot (\kappa_0 \vec{\nabla} P_0) \quad (16)$$

257

Remembering that  $\vec{\nabla} P_0 = 0$ , Eq. (16) becomes:

$$-\frac{1}{\gamma P_0} \frac{dP_0}{dt} = \vec{\nabla} \cdot \vec{u}_0 \quad (17)$$

258

259

260

261

262

263

264

265

266

that degenerates into the classical divergent constraint for incompressible flow,  $\vec{\nabla} \cdot \vec{u}_0 = 0$ , when assuming a constant background pressure  $P_0$  or at steady-state. Thus, at steady-state, the velocity fluctuations will be of the order of the Mach number.

The above results show that the choice  $Re_\infty = Pr_\infty = 1$  conserves the low Mach asymptotic limit. Thus, it remains to determine the scaling of the normalization parameter  $n(P)$ . In the case under consideration, the viscosity coefficients  $\mu$  and  $\kappa$  are set equal. Using the definition of the viscosity coefficient in Eq. (10) it can be shown that:

$$\mu_\infty = \frac{\rho_\infty c_\infty^2 u_\infty L}{n_{P,\infty}} \quad (18)$$

267 where  $n_{P,\infty}$  is the far-field quantity for the normalization parameter  $n_P$ .  
 268 Substituting Eq. (18) into Eq. (13) and remembering that the numerical  
 269 Reynolds number scales as one by assumption, it yields:

$$n_{P,\infty} = \rho_\infty c_\infty^2 \quad (19)$$

270 Eq. (19) tells us that in the asymptotic limit, the normalization parameter  
 271  $n_P$  scales as  $\rho_\infty c_\infty^2$  which leaves us with two options: either  $n_P = \rho c^2$  or  
 272  $n_P = P$ . The choice was made to use  $n_P = \rho c^2$  in the low Mach asymptotic  
 273 limit: it was found to behave well and the pressure can become locally  
 274 negative and null in some particular case as shown in Section 5.

275 •  $Re_\infty = Pr_\infty = M_\infty$  or  $m = n = 1$ :  
 276 The reasoning leading to the derivation of the asymptotic equations is  
 277 similar to the previous case. Thus, only the mains step are given. The  
 278 asymptotic equations obtained with the condition  $Re_\infty = Pr_\infty = M_\infty$  are  
 279 the following:

At order  $M_\infty^{-2}$ :

$$\vec{\nabla} P_0 = 0$$

At order  $M_\infty^{-1}$ :

$$\vec{\nabla} P_1 = \vec{\nabla} \cdot (\mu_0 \rho_0 \vec{\nabla}^s \vec{u}_0 + \kappa_0 \vec{u}_0 \vec{\nabla} \rho_0)$$

At order 1:

$$\partial_t \rho_0 + \vec{\nabla} \cdot (\rho_0 \vec{u}_0) = \vec{\nabla} \cdot (\kappa \vec{\nabla} \rho)_1$$

$$\partial_t (\rho_0 \vec{u}_0) + \vec{\nabla} \cdot (\rho_0 \vec{u}_0 \otimes \vec{u}_0) + \vec{\nabla} P_2 = \vec{\nabla} \cdot (\rho \mu \vec{\nabla}^s \vec{u} + \kappa \vec{u} \otimes \vec{\nabla} \rho)_1$$

$$\partial_t (\rho_0 E_0) + \vec{\nabla} \cdot [\vec{u}_0 (\rho_0 E_0 + P_0)] = \vec{\nabla} \cdot (\kappa \vec{\nabla} (\rho e))_1$$

280 Unlike the previous case, only the leading-order pressure  $P_0$  is spatially  
 281 constant. Thus, the pressure fluctuations are expected to be of the order  
 282 of the Mach number instead of the Mach number square as predicted:  
 283  $P(\vec{x}, t) = P_0(t) + M_\infty P_1(\vec{x}, t) + M_\infty^2 P_2(\vec{x}, t)$ . Using the equation of state,  
 284 the order 1 of the energy equation can be recast as follows:

$$(\gamma - 1) \partial_t P_0 + \gamma P_0 \vec{\nabla} \cdot \vec{u}_0 = (\gamma - 1) \vec{\nabla} \cdot (\kappa_0 \vec{\nabla} P_1) \quad (20)$$

285 Thus, at steady-state, in the presence of pressure fluctuation in the first-  
 286 order pressure  $P_1$ , the divergence constraint from the asymptotic analysis  
 287  $\vec{\nabla} \cdot \vec{u}_0 = 0$  is not satisfied. By choosing the Reynolds and Prandtl numbers  
 288 equal to the Mach number, the multi-D Euler equations do not seem to  
 289 converge to the incompressible equations in the low Mach asymptotic limit.  
 290 The scaling of the normalization parameters that matches the condition  
 291  $Re_\infty = Pr_\infty = M_\infty$  is derived on the same model as before:

$$n_{P,\infty} = \rho_\infty u_\infty c_\infty \quad (21)$$

292 which imposes  $n(P) = \rho c \|\vec{u}\|$ .

- $Re_\infty = M_\infty$  and  $Pr_\infty = 1$  or  $m = 1$  and  $n = 0$ :

For this particular case, the viscosity coefficients  $\mu$  and  $\kappa$  are not set equal. Therefore, two normalization parameters have to be determined. The details of the derivation are given in appendix (not done yet). The correct low Mach asymptotic limit was recovered with the choice  $Re_\infty = M_\infty$  and  $Pr_\infty = 1$ .

This normalization parameter is only valid in the asymptotic limit and the purpose of this paper is to define a viscosity coefficient  $\mu$  that is valid for a wide range of Mach numbers. Thus, it is proposed to define the high-order viscosity coefficient  $\mu_e$  as follows:

$$\mu_e = h^2 \frac{\max(\tilde{D}_e, J)}{(1 - f(M))g(P) + f(M)\rho||\vec{u}||^2} \quad (22)$$

where  $f(M)$  is a function of the local Mach number  $M$  with the following properties:

$$\begin{cases} f(M) \rightarrow 0 \text{ as } M \rightarrow 0 \\ f(M) \rightarrow 1 \text{ as } M \geq 1 \end{cases} \quad (23)$$

and  $g(P)$  has the following definition:

$$\begin{cases} g(P) = \rho c^2 \text{ if } Re_\infty = Pr_\infty = 1 \\ g(P) = \rho c ||\vec{u}|| \text{ if } Re_\infty = Pr_\infty = M_\infty \end{cases} \quad (24)$$

The choice of the function  $f(M)$  is not fixed and a few examples are available in the literature. A simple definition is  $f(M) = \min(M, 1)$  which meets the conditions of Eq. (23). Another definition for  $f(M)$  was proposed by [12]. All of the numerical results presented in Section 5 were obtained by using  $f(M) = \min(M, 1)$  which is simple to implement. A convergence test for a subsonic flow over a 2-D cylinder will show that this definition of  $f(M)$  yields the correct behavior in the asymptotic limit. The definition of the high-order viscosity coefficient  $\mu_e(\vec{r}, t)$  should behave well for complex flow where a near incompressible regime coexists with a supersonic flow domain since  $f(M)$  is function of the local Mach number.

For clarity purpose, the full definition of the viscosity coefficient  $\mu(\vec{r}, t)$  is recalled:

$$\begin{cases} \mu(\vec{r}, t) = \max(\mu_{max}(\vec{r}, t), \mu_e(\vec{r}, t)) \\ \text{where } \mu_{max}(\vec{r}, t) = \frac{h}{2} (||\vec{u}|| + c) \\ \text{and } \mu_e(\vec{r}, t) = h^2 \frac{\max(\tilde{D}_e, J)}{(1 - f(M))g(P) + f(M)\rho||\vec{u}||^2} \\ \mu(\vec{r}, t) = \kappa(\vec{r}, t) \end{cases} \quad (25)$$

These viscosity coefficients are valid for both the multi-D Euler equations with variable and constant area and are employed with the dissipative terms detailed in Eq. (15). The reader will notice that, through the derivation, none assumption was made on the type of equation of state besides the convexity condition on the entropy function  $s$ . The remaining of this paper (Section 5) will focus on demonstrating that the definition of the viscosity coefficient given in Eq. (25) is indeed well-scaled in the asymptotic limit and that shocks are still well resolved.

## 325 4. Solution Techniques Spatial and Temporal Discretizations

326 In order to detail the partial and temporal discretization used for this study,  
 327 the system of equations Eq. (7) is considered under the following form for sim-  
 328 plicity:

$$\partial_t U + \vec{\nabla} \cdot F(U) = S \quad (26)$$

329 where  $U$  is the vector solution,  $F$  is a conservative vector flux and  $S$  is a vector  
 330 source that can contain the non-conservative term  $P\vec{\nabla}A$ .

### 331 4.1. Spatial and Temporal Discretizations

332 The system of equation given in Eq. (26) is discretized using a continuous  
 333 Galerkin finite element method and high-order temporal integrators provided  
 334 by the MOOSE framework.

#### 335 4.1.1. CFEM

336 In order to apply the continuous finite element method, Eq. (26) is multiplied  
 337 by a smooth test function  $\phi$ , integrated by part and each integral is split onto  
 338 each finite element  $e$  of the discrete mesh  $\Omega$  bounded by  $\partial\Omega$ , to obtain a weak  
 339 solution:

$$\sum_e \int_e \partial_t U \phi - \sum_e \int_e F(U) \cdot \vec{\nabla} \phi + \int_{\partial\Omega} F(U) \vec{n} \phi - \sum_e \int_e S \phi = 0 \quad (27)$$

340 The integrals over the elements  $e$  are evaluated using quadrature-point rules.  
 341 The Moose framework provides a wide range of test function and quadrature  
 342 rules: trapezoidal and Gauss rules among others. Linear Lagrange polynomials  
 343 will be used as test functions and should ensure second-order convergence for  
 344 smooth functions. The order of convergence will be demonstrated.

#### 345 4.1.2. Temporal integrator

346 The MOOSE framework offers both first- and second-order explicit and im-  
 347 plicit temporal integrators. In all of the numerical examples presented in Sec-  
 348 tion 5, the time-dependent term  $\int_e \partial_t U \phi$  will be evaluated using the second-order  
 349 temporal integrator BDF2. By considering three solutions,  $U^{n-1}$ ,  $U^n$  and  $U^{n+1}$   
 350 at three different time  $t^{n-1}$ ,  $t^n$  and  $t^{n+1}$ , respectively, it yields:

$$\begin{aligned} \int_e \partial_t U \phi &= \int_e (\omega_0 U^{n+1} + \omega_1 U^n + \omega_2 U^{n-1}) \phi & (28) \\ \text{with } \omega_0 &= \frac{2\Delta t^{n+1} + \Delta t^n}{\Delta t^{n+1} (\Delta t^{n+1} + \Delta t^n)}, \\ \omega_1 &= -\frac{\Delta t^{n+1} + \Delta t^n}{\Delta t^{n+1} \Delta t^n} \\ \text{and } \omega_2 &= \frac{\Delta t^{n+1}}{\Delta t^n (\Delta t^{n+1} + \Delta t^n)} \end{aligned}$$

351 where  $\Delta t^n = t^n - t^{n-1}$  and  $\Delta t^{n+1} = t^{n+1} - t^n$ .

#### 352 4.2. Boundary conditions

353 The boundary conditions will be treated by either using Dirichlet or Neu-  
 354 mann conditions. The multi-D Euler equations are wave-dominated systems  
 355 that require great care when dealing with boundary conditions. It is often rec-  
 356 ommended to use the characteristic equations to compute the correct flux at the  
 357 boundaries. Our implementation of the subsonic boundary conditions will fol-  
 358 low the method described in [19] that was developed for Ideal Gas and Stiffened  
 359 Gas equation of states. For each numerical solution presented in Section 5, the  
 360 type of boundary conditions used will be specified and taken among the follow-  
 361 ings: supersonic inlet, subsonic inlet (stagnation pressure boundary), supersonic  
 362 outlet and subsonic inlet (static pressure boundary).

#### 363 4.3. Solver

364 A Free-Jacobian-Newton-Krylov (FJNK) method is used to solve for the  
 365 solution at each time step. The jacobian matrix of the discretized equations  
 366 was derived by hand, hard coded and used as a preconditioner. This method  
 367 requires the partial derivative of the pressure with respect to the conservative  
 368 variables to be known. The contribution of the artificial dissipative terms to  
 369 the jacobian matrix is simplified by assuming constant viscosity coefficients as  
 370 shown in Eq. (29) for the dissipative terms of the continuity equation:

$$\frac{\partial}{\partial U_i} \left( \kappa \vec{\nabla} \rho \vec{\nabla} \phi \right) = \kappa \frac{\partial}{\partial U_i} (\rho) \vec{\nabla} \phi \quad (29)$$

371 where  $U_i$  denotes the set of conservative variables.

### 372 5. Numerical Results

373 This section is dedicated to presenting 1- and 2-D numerical results obtained  
 374 by solving Eq. (7) with the entropy viscosity method. This section has two ob-  
 375 jectives: validate our new definition of the viscosity coefficients for the low Mach  
 376 limit, and, make sure that the new definition can still resolve shocks.

377 The first set of 1-D simulations consist of liquid water and steam flowing in  
 378 a convergent-divergent nozzle. This test is interesting for multiple reasons: a  
 379 steady-state is reached (some stabilization methods are known to have difficul-  
 380 ties to reach a steady-state ([3, 4]), it can be performed for liquid and gas phases,  
 381 and, an analytical solution of the steady-state solution is available which allow  
 382 for convergence study. The 1-D Leblanc shock tube test [21] (in a straight pipe)  
 383 is also performed and consists of a flow developing shocks. A convergence study  
 384 will be performed in order to demonstrate convergence of the numerical solution  
 385 to the exact solution.

386 This section also included 2-D simulations from subsonic to supersonic flows.  
 387 Subsonic flows of a gas over a 2-D cylinder and a hump [22] are simulated and  
 388 results are shown for various far-field Mach numbers. Numerical results of a su-  
 389 personic flow in a compression corner are provided to illustrate the capabilities  
 390 of the new definition in the supersonic case. Convergence studies are performed

when an analytical solution is available.  
 For each simulation, informations relative to the boundary conditions and the equation of state will be provided. All of the numerical solution presented in this section are run with the second-order temporal integrator *BDF2* and linear polynomials test functions. The integrals are numerically computed using a second-order Gauss quadrature rule. The Ideal Gas [23] or Stiffened Gas equation of state [24] are used and a generic formulation is recalled in Eq. (30).

$$P = (\gamma - 1)\rho(e - q) - \gamma P_\infty \quad (30)$$

where the parameters  $q$  and  $P_\infty$  are fluid dependent and will be specified in time. Eq. (30) degenerates to the Ideal Gas equation of state by setting  $q$  and  $P_\infty$  to zero. The Ideal and Stiffened Gas equation of states have a convex entropy  $s$ :

$$s = C_v \ln \left( \frac{P + P_\infty}{\rho^{\gamma-1}} \right)$$

#### 5.1. Liquid water in a 1-D divergent-convergent nozzle

The simulation consists of liquid water flowing through a 1-D convergent-divergent nozzle with the following equation,  $A(x) = 1 + 0.5 \cos(2\pi x/L)$ , where  $L = 1m$  is the length of the nozzle. At the inlet, the stagnation pressure and temperature are set to  $P_0 = 1MPa$  and  $T_0 = 453K$ , respectively. At the outlet, only the static pressure is specified:  $P_s = 0.5MPa$ . Details about the theory related to the inlet and outlet boundary conditions can be found in [19]. Initially, the temperature is uniform and set equal to the stagnation temperature and the pressure linearly decreases from the stagnation pressure to the static one. Finally, the liquid is assumed at rest. The Stiffened Gas equation of state is used to model the liquid water with the parameters provided in Table 1.

Table 1: Stiffened Gas Equation of State parameters for liquid water.

$\gamma$	$C_v (J \cdot kg^{-1} \cdot K^{-1})$	$P_\infty (Pa)$	$q (J \cdot kg^{-1})$
2.35	1816	$10^9$	$-1167.10^3$

Because of the low pressure difference between the inlet and the outlet, and the large value of  $P_\infty$ , the flow remains subsonic and thus, should not display any shock. Enthalpy and entropy are conserved through the nozzle, and these conservation relations are used to determine the exact solution at steady-state [25]. Plots of the velocity, density and pressure are given at steady-state in Fig. 1a, Fig. 1b, Fig. 1c, respectively, along with the exact solution for comparison. The viscosity coefficients are also plotted in Fig. 1d. The mesh used is uniform and has 50 cells.

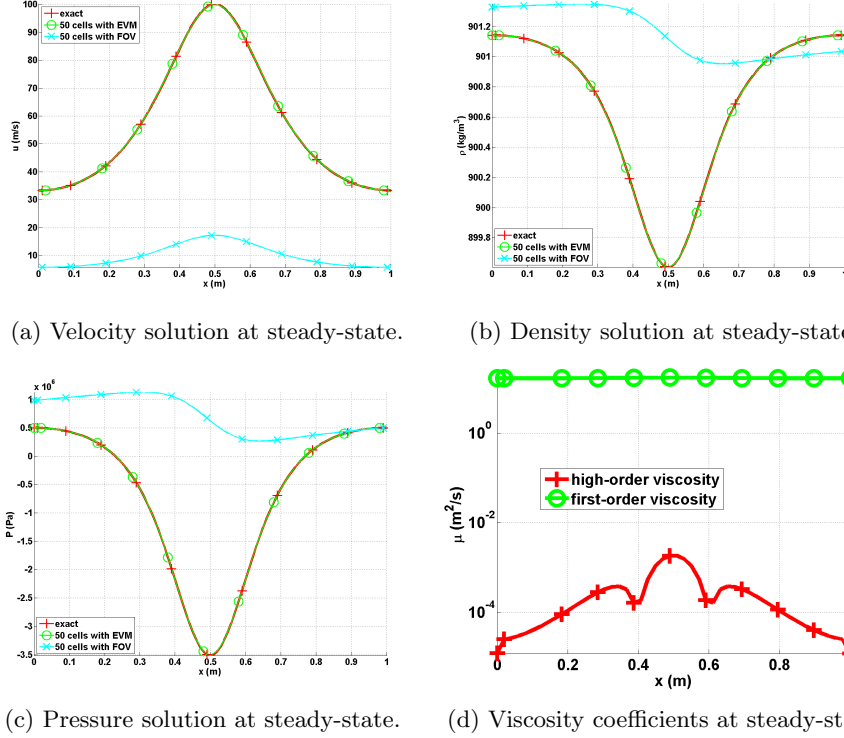


Figure 1: Steady-state solution for liquid phase in a 1-D convergent-divergent nozzle with an uniform mesh of 50 cells.

In Fig. 1, the numerical solutions of the pressure, velocity and density obtained with the first-order viscosity (FOV) and the entropy viscosity method (EVM) are plotted against the exact solution. A fairly coarse mesh (50 cells) was used. The numerical solution obtained with the EVM and the exact solution perfectly overlap. On the other hand, the numerical solution run with the FOV does not give the correct steady-state: this is an illustration of the effect of ill-scaled dissipative terms. It is also noted that the second-order viscosity coefficient is very small compare to the first-order one as expected (Fig. 1d): (i) the numerical solution is smooth as shown in Fig. 1 and (ii) the flow is in a low Mach regime and thus isentropic. A convergence study was performed using the exact solution as a reference: the L1 and L2 norms of the error and the corresponding convergence rates are computed at steady-state on various uniform mesh from 4 to 256 cells. The results for linear polynomials  $Q_1$  are reported in Table 2 and Table 3 for the primitive variables: density, velocity and pressure.

Table 2: L1 norm of the error for the liquid phase in a 1-D convergent-divergent nozzle at steady-state.

cells	density	rate	pressure	rate	velocity	rate
4	$2.8037 \cdot 10^{-1}$	—	$8.4705e \cdot 10^5$	—	7.2737	—
8	$1.3343 \cdot 10^{-1}$	1.0713	$4.7893e \cdot 10^5$	0.24227	6.1493	0.074683
16	$2.9373 \cdot 10^{-2}$	2.1835	$1.0613e \cdot 10^5$	2.3247	1.2275	2.4501
32	$5.1120 \cdot 10^{-3}$	2.5225	$1.8446 \cdot 10^4$	2.6959	$1.8943 \cdot 10^{-1}$	3.0966
64	$1.0558 \cdot 10^{-3}$	2.2755	$3.7938 \cdot 10^3$	2.3207	$3.7919 \cdot 10^{-2}$	2.3323
128	$2.3712 \cdot 10^{-4}$	2.1547	$8.4471 \cdot 10^2$	2.0624	$8.5517 \cdot 10^{-3}$	2.0473
256	$5.6058 \cdot 10^{-5}$	2.0806	$1.9839 \cdot 10^2$	2.0478	$2.0475 \cdot 10^{-3}$	1.9833
512	$1.3278 \cdot 10^{-5}$	2.0778	46.622	2.0478	$4.9516 \cdot 10^{-4}$	1.9669

Table 3: L2 norm of the error for the liquid phase in a 1-D convergent-divergent nozzle at steady-state.

cells	density	rate	pressure	rate	velocity	rate
4	$3.106397 \cdot 10^{-1}$	—	$5.254445 \cdot 10^5$	—	3.288543	—
8	$7.491623 \cdot 10^{-2}$	2.07	$1.636966 \cdot 10^5$	1.60	1.823880	0.90
16	$2.079858 \cdot 10^{-2}$	1.80	$4.627338 \cdot 10^4$	1.75	$4.990605 \cdot 10^{-1}$	1.83
32	$5.329627 \cdot 10^{-3}$	1.90	$1.180287 \cdot 10^4$	1.92	$1.261018 \cdot 10^{-1}$	1.93
64	$1.341583 \cdot 10^{-3}$	1.94	$2.967104 \cdot 10^3$	1.98	$3.160914 \cdot 10^{-2}$	1.99
128	$3.359766 \cdot 10^{-4}$	1.99	$7.428087 \cdot 10^2$	1.99	$7.907499 \cdot 10^{-3}$	1.99
256	$8.403859 \cdot 10^{-5}$	1.99	$1.857861 \cdot 10^2$	1.99	$1.977292 \cdot 10^{-3}$	1.99
512	$2.10075 \cdot 10^{-5}$	1.99	27.048	1.99	$4.9516 \cdot 10^{-4}$	1.99

435 It is observed that the convergence rate for the L1 and L2 norm of the error  
436 is 2: the entropy viscosity method conserves the high-order accuracy when the  
437 numerical solution is smooth, and the new definition of the entropy viscosity  
438 coefficient seems to behave as expected in the low Mach limit.

## 439 5.2. Steam in a 1-D divergent-convergent nozzle

440 Instead of liquid water, we now simulate a flow of steam using the exact same  
441 1-D geometry, initial conditions and boundary conditions as in Section 5.1. The  
442 Stiffened gas equation of state is still used but with different parameters that are  
443 given in Table 4: steam is a gas and compressible effects will become dominant.

Table 4: Stiffened Gas Equation of State parameters for steam.

$\gamma$	$C_v \text{ (} J \cdot kg^{-1} \cdot K^{-1} \text{)}$	$P_\infty \text{ (Pa)}$	$q \text{ (} J \cdot kg^{-1} \text{)}$
1.43	1040	0	$2030 \cdot 10^3$



444 The pressure difference applied between the inlet and outlet is large enough  
 445 to make the steam accelerates through the nozzle and result in the formation of  
 446 shock in the divergent part. The behavior is different from what is observed for  
 447 the liquid water phase in Section 5.1 because of the liquid to gas density ratio  
 448 that is of 1000. Even though a shock forms, an exact solution at steady-state  
 449 is still available [25]. The objective of this section is to show that using the  
 450 new definition of the viscosity coefficient in Eq. (25), the shock can be correctly  
 451 resolved without spurious oscillation. The steady-state numerical solution is  
 452 shown in Fig. 2 and was run with a mesh of 1600 cells.

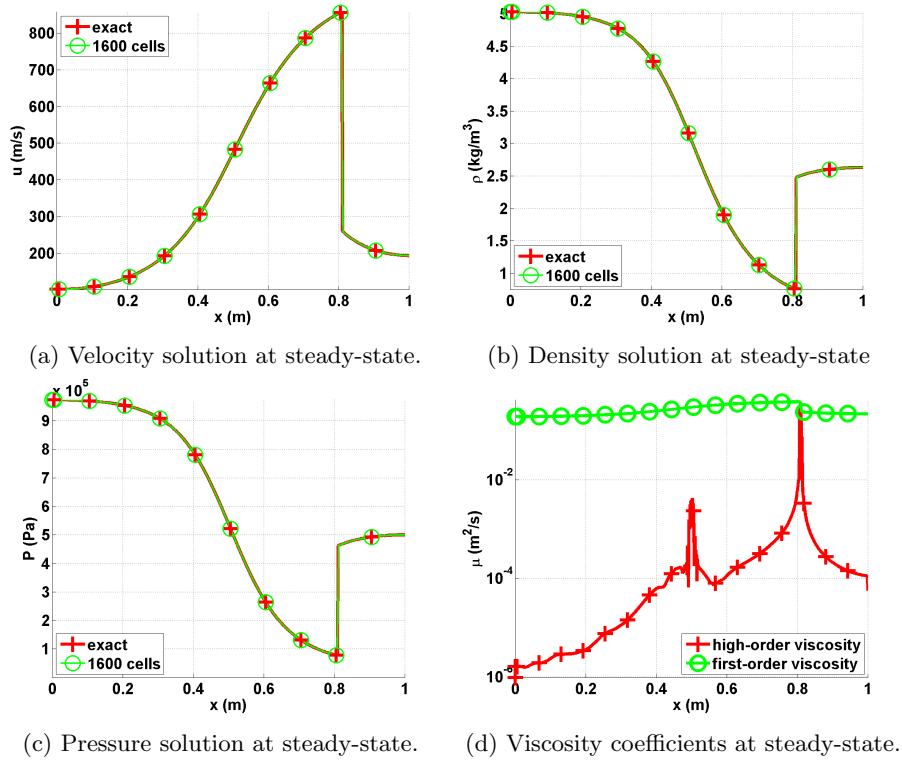


Figure 2: Steady-state solution for vapor phase in a 1-D convergent-divergent nozzle.

453 The steady-state solution of the density, velocity and pressure are given  
 454 in Fig. 2a, Fig. 2b and Fig. 2c. The steady-solution displays a shock around  
 455  $x = 0.8m$  and match the exact solution. In Fig. 2d, the first- and second-  
 456 order viscosity coefficients are log plotted at steady-state: the second-order  
 457 viscosity coefficient is peaked in the shock region around  $x = 0.8m$  as expected,  
 458 and saturate to the first-order viscosity coefficient. The profile also displays  
 459 another peak at  $x = 0.5m$  that corresponds to the position of the sonic point

for a 1-D convergent-divergent nozzle: this particular point is known to develop small instabilities that are detected when computing the jumps of the pressure and density gradients. Anywhere else, the second-order viscosity coefficient is small. In order to prove convergence of the numerical solution to the exact solution, a convergence study is performed. Because of the presence of a shock, second-order accuracy cannot be achieved. However, the convergence rate of a numerical solution containing a shock is known and expected to be of 1 and 1/2 when computing the L1 and L2 norms of the error, respectively (see Theorem 9.3 in [26]). Results are reported in Table 5 and Table 6 for the primitive variables: density, velocity and pressure.

Table 5: L1 norm of the error for the vapor phase in a 1-D convergent-divergent nozzle at steady-state.

cells	density	rate	pressure	rate	velocity	rate
5	$0.72562 \cdot 10^{-1}$	—	$1.5657 \cdot 10^5$	—	173.69	—
10	$0.4165 \cdot 10^{-1}$	0.80088	$9.6741 \cdot 10^4$	0.63425	120.69	0.52519
20	$0.20675 \cdot 10^{-1}$	1.0104	$4.9193 \cdot 10^4$	0.96971	72.149	0.74228
40	$0.093703 \cdot 10^{-1}$	1.1417	$2.0103 \cdot 10^4$	0.72728	34.716	1.0554
80	$0.047328 \cdot 10^{-1}$	0.9854	$1.0208 \cdot 10^4$	0.9777	16.082	1.1101
160	$0.023965 \cdot 10^{-2}$	0.9817	$5.1969 \cdot 10^3$	0.9739	7.9573	1.0150
320	$0.020768 \cdot 10^{-2}$	0.9886	$2.5116 \cdot 10^3$	1.0490	3.7812	1.0734
640	$0.0059715 \cdot 10^{-2}$	1.0160	$1.2754 \cdot 10^3$	0.9776	1.8353	1.0428

Table 6: L2 norm of the error for the vapor phase in a 1-D convergent-divergent nozzle at steady-state.

cells	density	rate	pressure	rate	velocity	rate
5	$9.7144 \cdot 10^{-1}$	—	$2.0215 \cdot 10^5$	—	236.94	—
10	$5.9718 \cdot 10^{-1}$	0.70195	$1.3024 \cdot 10^5$	0.63425	166.56	0.50854
20	$2.9503 \cdot 10^{-1}$	1.0173	$6.6503 \cdot 10^4$	0.96971	103.36	0.68831
40	$1.8193 \cdot 10^{-1}$	0.69747	$4.0171 \cdot 10^4$	0.72728	66.374	0.6390
80	$1.3366 \cdot 10^{-1}$	0.44485	$2.3163 \cdot 10^4$	0.43576	42.981	0.62692
160	$9.6638 \cdot 10^{-2}$	0.46790	$1.7263 \cdot 10^4$	0.42413	31.717	0.43844
320	$7.0896 \cdot 10^{-2}$	0.44688	$1.2763 \cdot 10^4$	0.43571	23.138	0.45499
640	$5.2191 \cdot 10^{-2}$	0.44190	$9.4217 \cdot 10^3$	0.43790	16.910	0.45238

The convergence rates for the L1 and L2 norms of the error are close to the theoretical values which prove convergence of the numerical solution to the exact solution.

473 *5.3. Leblanc shock tube*

474 The 1-D Leblanc shock tube is a Riemann problem designed to test the  
 475 robustness and the accuracy of the stabilization method. The initial conditions  
 476 are given in Table 7. The ideal gas equation of state is used to compute the  
 477 fluid pressure with the following heat capacity ratio  $\gamma = 5/3$ .

Table 7: Initial conditions for the 1-D Leblanc shock tube.

	$\rho$	$u$	$e$
left	1.	0.	0.1
right	$10^{-3}$	0.	$10^{-7}$

478 This test is computationally challenging because of the large left to right  
 479 pressure ratio. The computational domain consists of a 1-D pipe of length  
 480  $L = 9m$  with an interface located at  $x = 2m$ . At  $t = 0.s$ , the interface is  
 481 removed, allowing the fluid to move. The numerical solution is run until  $t = 4.s$   
 482 and the density, momentum and total energy profiles are given in Fig. 3a, Fig. 3b  
 483 and Fig. 3c, respectively, along with the exact solution. The viscosity coefficients  
 484 are also plotted in Fig. 3d. These plots were run with three different uniform  
 485 mesh of 800, 3200 and 6000 cells and a constant time step  $\Delta t = 10^{-3}s$ .

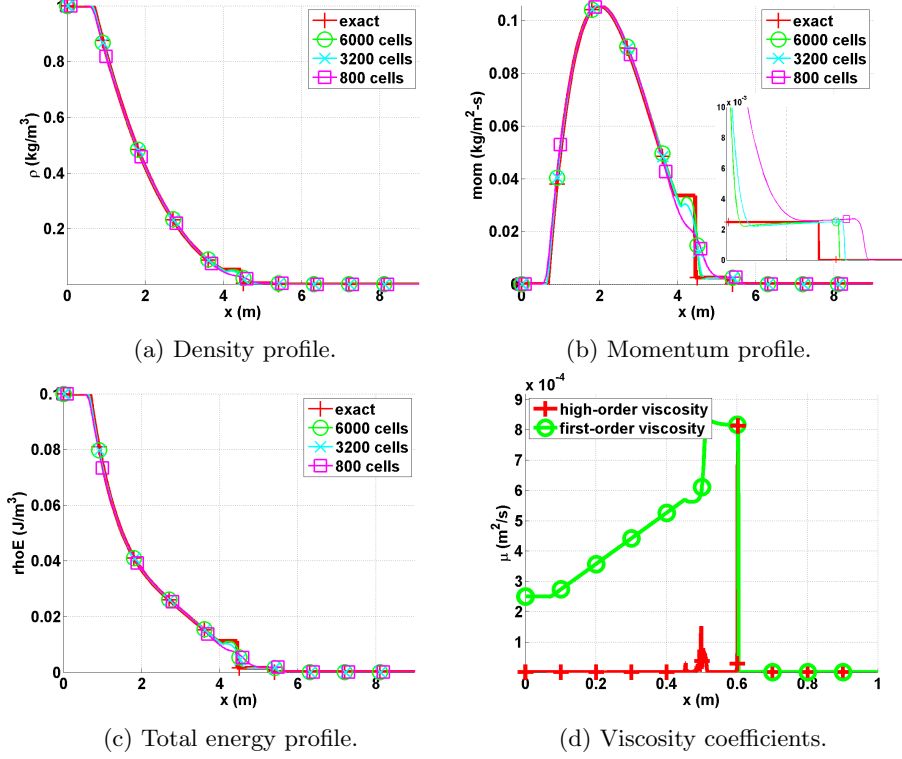


Figure 3: Numerical solution for the 1-D Leblanc shock tube at  $t = 4.s$ .

486 The density, momentum and total energy profiles given in Fig. 3 do not  
 487 display any oscillations. In Fig. 3b, the shock region is zoomed in for better  
 488 resolution: the shock is well resolved and do not show any oscillation. It is  
 489 also observed that the shock position of the numerical solution converges to the  
 490 exact position when refining the mesh. The contact wave is shown in Fig. 3b at  
 491  $x = 4.5m$ . The second-order viscosity coefficient profile is shown in Fig. 3d and  
 492 behaves as expected: it saturates to the first-order viscosity in the shock region  
 493 and thus prevent oscillations from forming. In the contact wave at  $x = 4.5m$ , a  
 494 smaller peak is observed that is due to the presence of the jumps in the definition  
 495 of the second-order viscosity coefficient (Eq. (25)).  
 496 Once again, a convergence study is performed in order to prove convergence of  
 497 the numerical solution to the exact solution. As for the vapor phase in the 1-D  
 498 nozzle (Section 5.2), the expected convergence rate for the L1 and L2 norms  
 499 of the error are 1 and 1/2, respectively. The exact solution was obtained by  
 500 running a 1-D Riemann solver and used as a reference solution to compute the  
 501 L1 and L2-norms of the error that are reported in Table 8 and Table 9 for the  
 502 conservative variables: density, momentum and total energy.

Table 8: L1 norm of the error for the 1-D Leblanc test at  $t = 4.s$ .

cells	density	rate	momentum	rate
100	$1.0354722 \cdot 10^{-2}$	—	$3.5471714 \cdot 10^{-3}$	—
200	$7.2680512 \cdot 10^{-3}$	0.51064841	$2.5933119 \cdot 10^{-3}$	0.45187331
400	$5.0825628 \cdot 10^{-3}$	0.51601245	$2.0668092 \cdot 10^{-3}$	0.32739054
800	$3.4025056 \cdot 10^{-3}$	0.57895861	$1.4793838 \cdot 10^{-3}$	0.48240884
1600	$2.1649953 \cdot 10^{-3}$	0.65223363	$9.7152832 \cdot 10^{-4}$	0.6066684
3200	$1.2465433 \cdot 10^{-3}$	0.79643094	$5.5937409 \cdot 10^{-4}$	0.79644263
6400	$6.4476928 \cdot 10^{-4}$	0.95107804	$3.0244198 \cdot 10^{-4}$	0.88715502
12800	$3.3950948 \cdot 10^{-4}$	0.92533116	$1.5958118 \cdot 10^{-4}$	0.9223679

cells	total energy	rate
100	0.0014033046	—
200	$9.8611746 \cdot 10^{-4}$	0.5089968
400	$7.7844421 \cdot 10^{-4}$	0.34116585
800	$5.5702549 \cdot 10^{-4}$	0.48285029
1600	$3.5720171 \cdot 10^{-4}$	0.64100438
3200	$2.0491799 \cdot 10^{-4}$	0.80169235
6400	$1.0914891 \cdot 10^{-4}$	0.90874889
12800	$5.7909794 \cdot 10^{-5}$	0.91441847

Table 9: L2 norm of the error for the 1-D Leblanc test at  $t = 4.s$ .

cells	density	rate	momentum	rate
100	$5.7187851 \cdot 10^{-3}$	—	$1.7767236 \cdot 10^{-3}$	—
200	$3.8995238 \cdot 10^{-3}$	0.55241073	$1.4913161 \cdot 10^{-3}$	0.25263314
400	$2.8103526 \cdot 10^{-3}$	0.4725468	$1.3305301 \cdot 10^{-3}$	0.164585
800	$2.1081933 \cdot 10^{-3}$	0.41474398	$1.1398931 \cdot 10^{-3}$	0.22310254
1600	$1.5731052 \cdot 10^{-3}$	0.42239201	$9.0394227 \cdot 10^{-4}$	0.33459602
3200	$1.0610667 \cdot 10^{-3}$	0.56809979	$6.2735595 \cdot 10^{-4}$	0.52694639
6400	$7.3309974 \cdot 10^{-4}$	0.53343397	$4.4545754 \cdot 10^{-4}$	0.49399631
12800	$5.1020991 \cdot 10^{-4}$	0.52291857	$3.1266758 \cdot 10^{-4}$	0.5106583

cells	total energy	rate
100	$7.6112265 \cdot 10^{-4}$	—
200	$5.5497308 \cdot 10^{-4}$	0.45571115
400	$4.6063172 \cdot 10^{-4}$	0.26880405
800	$3.7798953 \cdot 10^{-4}$	0.28526749
1600	$2.9584646 \cdot 10^{-4}$	0.35349763
3200	$2.054455 \cdot 10^{-4}$	0.52609289
6400	$1.4670834 \cdot 10^{-4}$	0.48580482
12800	$1.0299897 \cdot 10^{-5}$	0.51032105

503 The convergence rates are close to the expected values which prove conver-  
 504 gence of the numerical solution to the exact solution.

#### 505 5.4. Subsonic flow over a 2-D cylinder

506 The flow of a fluid over a 2-D cylinder is a typical benchmark case to test the  
 507 behavior of a numerical method in the low Mach regime. For this test, an ana-  
 508 lytical solution is available in the incompressible limit or low Mach limit (REFS)  
 509 and often referred to as potential flow. The main features of the potential flow  
 510 are the following:

- 511 • The solution is symmetric: the iso-mach number lines are used to asses  
 512 the symmetry of the numerical solution.
- 513 • The velocity at the top of the cylinder is twice the incoming velocity set  
 514 at the inlet.
- 515 • The pressure fluctuations are proportional to the inlet Mach number square,  
 516 as follows:

$$\tilde{P} = \frac{\max(P) - \min(P)}{\max(P)} \propto M_{\infty}^2$$

517 where  $\tilde{P}$  and  $M_{\infty}$  are the pressure fluctuations and the inlet Mach number,  
 518 respectively.

519 The computational domain consists of a  $1 \times 1$  square with a circular hole of radius  
 520 0.05 in its middle. At the inlet, a subsonic stagnation boundary condition is  
 521 used: the stagnation pressure and temperature are computed using the following  
 522 relations, valid for the Stiffened and Ideal gas equation of states:

$$\begin{cases} P_0 = P \left(1 + \frac{\gamma-1}{2} M^2\right)^{\frac{\gamma}{\gamma-1}} \\ T_0 = T \left(1 + \frac{\gamma-1}{2} M^2\right) \end{cases} \quad (31)$$

523 The static pressure  $P_s = 101325 \text{ Pa}$  is set at the subsonic outlet and a static  
 524 pressure boundary type is used. The implementation of the pressure boundary  
 525 conditions is done on the model of [19]. A solid wall boundary condition is set for  
 526 the top and bottom walls of the computational domain: the normal velocity is  
 527 zero since no mass can penetrate the solid body. The mesh is made of triangular  
 528 cells.

529 The steady-state for Mach numbers ranging from  $M_{\infty} = 10^{-3}$  to  $M_{\infty} = 10^{-7}$   
 530 is shown in Fig. 4. The iso-Mach lines are drawn with 50 intervals ranging from  
 531  $10^{-8}$  to  $2M_{\infty}$ , and allow to assess the symmetry of the numerical solution.

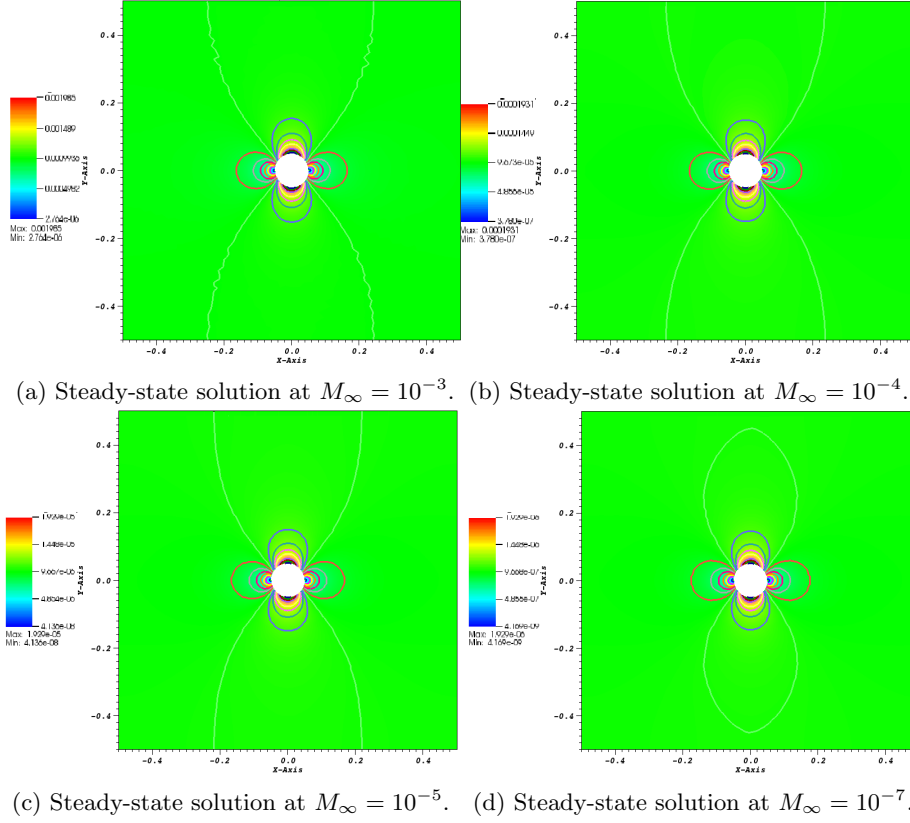


Figure 4: Steady-state solution for a subsonic flow over a 2-D cylinder.

532 In Table 10, the velocity at the top of the cylinder and at the inlet are given  
 533 for the different values of the Mach number presented in Fig. 4. The ratio of  
 534 the inlet velocity to the velocity at the top of cylinder is also computed and is  
 535 very close to 2 as expected.

Table 10: Velocity ratio for different Mach numbers.

Mach number	inlet velocity	velocity at the top of the cylinder	ratio
$10^{-3}$	$2.348 \cdot 10^{-3}$	$1.176 \cdot 10^{-3}$	1.99
$10^{-4}$	$2.285 \cdot 10^{-4}$	$1.145 \cdot 10^{-4}$	1.99
$10^{-5}$	$2.283 \cdot 10^{-5}$	$1.144 \cdot 10^{-5}$	1.99
$10^{-6}$	$2.283 \cdot 10^{-6}$	$1.144 \cdot 10^{-6}$	1.99
$10^{-7}$	$2.283 \cdot 10^{-7}$	$1.144 \cdot 10^{-7}$	1.99

536 In Fig. 5, the pressure and velocity fluctuations are plotted as a function  
 537 of the far field Mach number, on a log-log plot. The pressure and velocity

538 fluctuations are expected to be of the order of the Mach number square and  
 539 the Mach number, respectively. It is known that some stabilization methods,  
 540 alike upwind scheme [27], can produce pressure fluctuations with the wrong  
 541 order. The objective of Fig. 5 is to show that the new definition of the viscosity  
 542 coefficients yields the correct order in the low Mach limit for both the pressure  
 543 and velocity variables. For reference purpose, the function  $f(M) = M^2$  and  
 544  $f(M) = M$  are plotted.

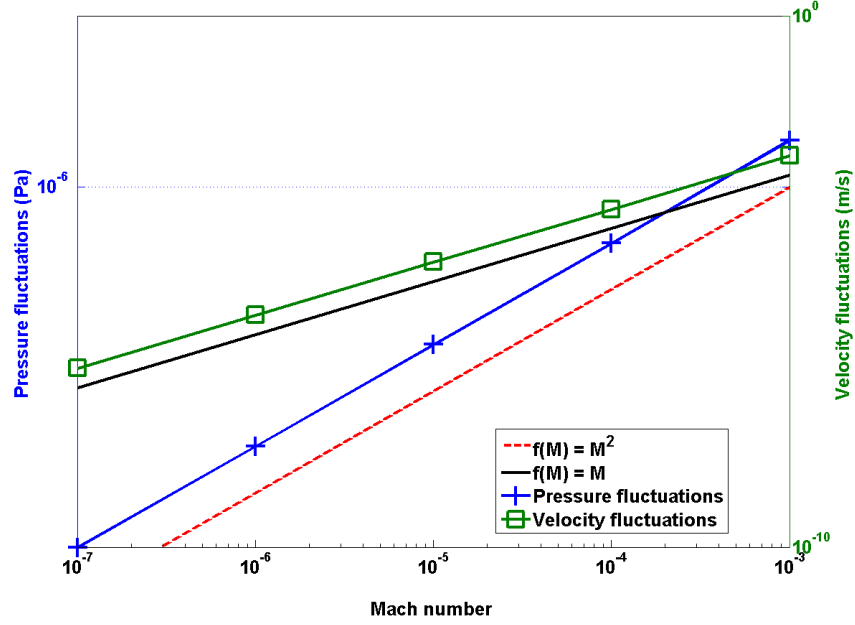


Figure 5: Log-log plot of the pressure and velocity fluctuations as a function of the far field Mach number.

#### 5.5. Subsonic flow over a 2-D hump

546 This is another example of an internal flow configuration. It consists of a  
 547 channel of height  $L = 1 \text{ m}$  and length  $3L$ , with a circular bump of length  $L$   
 548 and thickness  $0.1L$ . The bump is located on the bottom wall at a distance  $L$   
 549 from the inlet. The system is initialized with a uniform pressure  $P = 101325$   
 550  $\text{Pa}$  and temperature  $T = 300 \text{ K}$ . The initial velocity is computed from the  
 551 Mach number,  $M_\infty$ , the pressure, the temperature and the Ideal Gas equation  
 552 of state with the heat capacity  $C_v = 717 \text{ J/kg} \cdot \text{K}$  and the heat capacity ratio  
 553  $\gamma = 1.4$ . At the inlet, a subsonic stagnation boundary condition is used and the  
 554 stagnation pressure and temperature are computed using Eq. (31). The static  
 555 pressure  $P_s = 101325 \text{ Pa}$  is set at the subsonic outlet. A uniform grid is used to  
 556 get the numerical solution until steady-state is reached. The results are shown  
 557 in Fig. 6a, Fig. 6b, Fig. 6c and Fig. 6d for the inlet Mach numbers  $M_\infty = 0.7$ ,



558  $M_\infty = 0.01$ ,  $M_\infty = 10^{-4}$  and  $M_\infty = 10^{-7}$ , respectively. It is expected that,  
 559 within the low Mach number range, the solution does not depend on the Mach  
 560 number and is identical to the solution obtained with an incompressible flow  
 561 code. On the other hand, for a flow at  $M = 0.7$ , the compressible effects  
 562 become more important and shock can form.

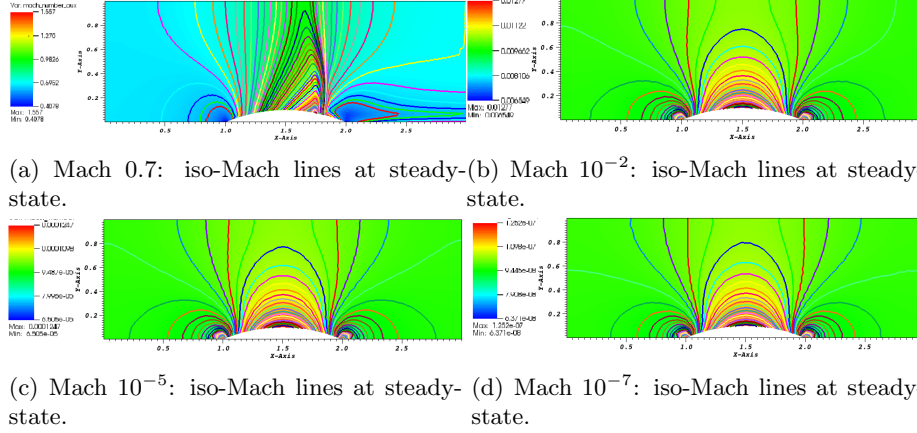


Figure 6: Steady-state solution for a 2-D flow over a circular bump.

563 The results showed in Fig. 6b, Fig. 6c and Fig. 6d correspond to the low  
 564 Mach regime. The iso-Mach lines are drawn ranging from the minimum and the  
 565 maximum of each legend with 50 intervals. The steady-state solution is sym-  
 566 metric and does not depend on the value of the inlet Mach number as expected.  
 567 In Fig. 6a, the steady-state numerical solution develops a shock: the compress-  
 568 ibility effect are no longer negligible. The iso-Mach lines are also plotted with  
 569 50 intervals and ranging from 0.4 to 1.6. The shock is well resolved and does  
 570 not display any instability or spurious oscillation.  
 571 The results presented in Fig. 6 were obtained with the new definition of the vis-  
 572 cosity coefficient (see Eq. (25)), and, illustrate the capabilities of the entropy-  
 573 viscosity method to adapt to the type of flow (subsonic and transonic flows)  
 574 without using any tuning parameters, but by just evaluating the entropy resid-  
 575 ual that is an indicator of the entropy production.

#### 5.6. Supersonic flow in a compression corner

577 This is an example of a supersonic flow over a wedge of angle  $15^\circ$  where an  
 578 oblique shock is generated at steady-state. The Mach number upstream of the  
 579 shock is fixed to  $M = 2.5$ . The initial conditions are uniform: the pressure and  
 580 temperature are set to  $P = 101325 \text{ Pa}$  and  $T = 300 \text{ K}$ , respectively. The initial  
 581 velocity is computed from the upstream Mach number and using the Ideal Gas  
 582 equation of state with the same parameters as in Section 5.5. The code is run  
 583 until steady-state. From the oblique shock theory [14], an analytical solution for  
 584 this supersonic flow is available and give the downstream to upstream pressure,

585 entropy and Mach number ratios. The analytical and numerical ratios are given  
586 in Table 11, and are very close. The shock wave angle at steady-state is also  
587 known and given by the so-called  $\theta - \beta - M$  relation:

$$\tan \theta = 2 \cot \beta \frac{M^2 \sin^2 \beta - 1}{M^2 (\gamma + \cos^2(2\beta)) + 2}$$

588 where  $\theta$ ,  $\beta$  and  $M$  denote the wedge angle, the shock wave angle and the up-  
589 stream Mach number, respectively. For the example under consideration with  
590 an inlet Mach number of 2.5, the exact value of the shock wave angle is of  $36.94^\circ$   
591 at steady-state. From Fig. 7a, the numerical value of the shock wave angle can  
592 be measured and is found equal to  $36.9^\circ$ : the numerical and exact values are  
593 very close.

Table 11: Analytical solution for the supersonic flow on an edge at  $15^\circ$  at  $M = 2.5$ .

	analytical downstream to upstream ratio	numerical downstream to upstream ratio
Pressure	2.47	2.467
Mach number	0.74	0.741
Entropy	1.03	1.026

594 The inlet is supersonic and therefore, the pressure, temperature and velocity  
595 are specified using Dirichlet boundary conditions. The outlet is also supersonic  
596 and none of the characteristics enter the domain through this boundary: the  
597 values will be computed by the implicit solver.

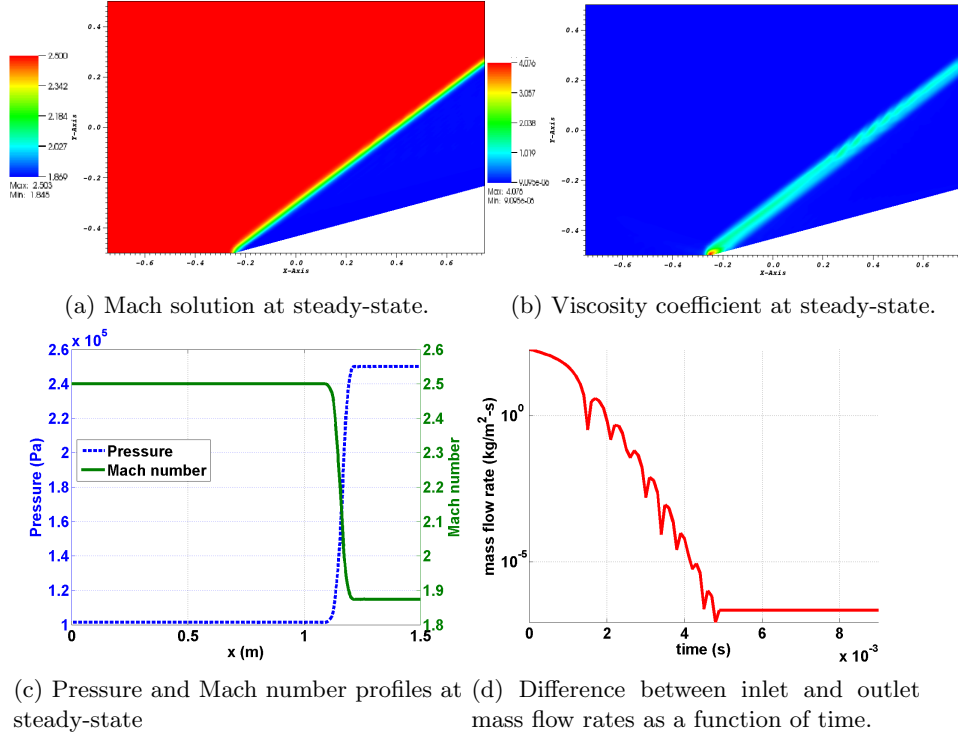


Figure 7: Steady-state solution for a flow in a 2-D compression corner.

The steady-state numerical solution is given in Fig. 7: the Mach number, the viscosity coefficients are plotted in Fig. 7a and Fig. 7b, respectively. The steady-state solution is formed of two regions of constant states, separated by the oblique shock. In Fig. 7b, the viscosity coefficient is large in the shock, small anywhere else, and thus, behaves as expected. At the corner of the edge at  $x = -0.25$  m, the viscosity coefficient is peaked because of the treatment of the wall boundary condition: at this particular node, the normal is not well defined and can cause numerical errors. The 1-D plots of the pressure and the mach number at  $y = 0$ , are also given in Fig. 7c: the shock does not show any spurious oscillations and is well resolved. Finally, the difference between the inlet and outlet mass flow rates is plotted in Fig. 7d and show that the steady-state is reached. Overall, the numerical solution does not show any oscillations, match the analytical solution, and the shock is well resolved.

## 6. Conclusions

A new version of the entropy viscosity method valid for a wide range of Mach number and applied to the multi-D Euler equations with variable area was derived and presented. The definition of the viscosity coefficient is now

616 consistent with the low Mach asymptotic limit, does not require an analytical  
 617 expression of the entropy function, and thus, could be used with any equation  
 618 of state having a convex entropy. Tests were performed with the Ideal and  
 619 Stiffened Gas equation of states. In 1-D, convergence of the numerical solu-  
 620 tion (either smooth or with shocks) to the exact solution was demonstrated by  
 621 computing the convergence rates of the L1 and L2 norms of the error for flows  
 622 in convergence-divergent nozzle and a straight pipe. 2-D simulations were also  
 623 performed for both subsonic and supersonic flows, and various geometries: the  
 624 entropy viscosity method behaves well for a wide range of Mach number. The  
 625 numerical results obtained for a flow over a circular bump (subsonic and tran-  
 626 sonic flows) illustrates the capabilities of the method to adapt to the flow type.  
 627 As future work, the entropy viscosity method will be extended to the 1-D seven  
 628 equations model [19]. This two-phase flow system of equations is a good can-  
 629 didate for two reasons: it is unconditionally hyperbolic and degenerates to the  
 630 multi-D Euler equations when one phase disappears.

## 631 Acknowledgments

632 The authors would like to thank Bojan Popov and Jean Luc Guermond for  
 633 the many fruitful discussions.

## 634 References

- 635 [1] J. L. Guermond, R. Pasquetti, Entropy viscosity method for nonlinear con-  
 636 servation laws, *Journal of Comput. Phys* 230 (2011) 4248–4267.
- 637 [2] J. L. Guermond, R. Pasquetti, Entropy viscosity method for high-order ap-  
 638 proximations of conservation laws, *Lecture Notes in Computational Science*  
 639 *and Engineering* 76 (2011) 411–418.
- 640 [3] B. Cockburn, C. Johnson, C. Shu, E. Tadmor, Advanced numerical approx-  
 641 imation of nonlinear hyperbolic equations, *Lecture Notes in Mathematics*  
 642 1697.
- 643 [4] B. Cockburn, G. Karniadakis, C. Shu, Discontinuous galerkin methods:  
 644 theory, computation and applications, *Lecture Notes in Computer Science*  
 645 *and Engineering* 11.
- 646 [5] R. Lohner, *Applied CFD Techniques: an Introduction based on Finite*  
 647 *Element Methods*, 2<sup>nd</sup> Edition Wiley, 2003.
- 648 [6] A. Lapidus, A detached shock calculation by second order finite differences,  
 649 *J. Comput. Phys.* 2 (1967) 154–177.
- 650 [7] R. Lohner, K. Morgan, J. Peraire, A simple extension to multidimensional  
 651 problems of the artificial viscosity due to lapidus, *Commun. Numer. Meth-*  
 652 *ods Eng.* 1(14) (1985) 141–147.

- 653 [8] J. Donea, A. Huerta, Finite Element Methods for Flow Problems, Oxford  
654 University Press, 2003.
- 655 [9] H. Guillard, C. Viozat, On the behavior of upwind schemes in the low mach  
656 number limit, *Computers & Fluids* 28 (1999) 63–86.
- 657 [10] E. Turkel, Preconditioned techniques in computational fluid dynamics,  
658 *Annu. Rev. Fluid Mech.* 31 (1999) 385–416.
- 659 [11] J. S. W. D. L. Darmofal, J. Peraire, The solution of the compressible euler  
660 equations at low mach numbers using a stabilized finite element algorithm,  
661 *Comput. Methods Appl. Mech. Engrg.* 190 (2001) 5719–5737.
- 662 [12] X.-S. Li, C.-W. Gu, An all-speed roe-type scheme and its asymptotic anal-  
663 ysis of low mach number behavior, *Journal of Computational Physics* 227  
664 (2008) 5144–5159.
- 665 [13] J. L. Guermond, B. Popov, Viscous regularization of the euler equations  
666 and entropy principles, under review.
- 667 [14] J. D. Anderson, Modern compressible flow, in: *Guide for Verification and*  
668 *Validation in Computational Solid Mechanic.*, New York, 1982, pp. 10–  
669 2006.
- 670 [15] J. L. Guermond, R. Pasquetti, Entropy-based nonlinear viscosity for four-  
671 rier approximations of conservation laws, in: *C.R. Math. Acad. Sci.*, Vol.  
672 326, Paris, 2008, pp. 801–806.
- 673 [16] V. Zingan, J. L. Guermond, J. Morel, B. Popov, Implementation of the  
674 entropy viscosity method with the discontinuous galerkin method, *Journal*  
675 *of Comput. Phys* 253 (2013) 479–490.
- 676 [17] E. F. Toro, *Riemann Solvers and numerical methods for fluid dynamics*,  
677 2<sup>nd</sup> Edition, Springer, 1999.
- 678 [18] B. Perthane, C. W. Shu, On positivity preserving finite volume schemes for  
679 euler equations, *Numer. Math.* 73 (1996) 119–130.
- 680 [19] R. Berry, R. Saurel, O. LeMetayer, The discrete equation method (dem)  
681 for fully compressible, two-phase flows in ducts of spatially varying cross-  
682 section, *Nuclear Engineering and Design* 240 (2010) 3797–3818.
- 683 [20] B. Muller, Low-mach number asymptotes of the navier-stokes equations,  
684 *Journal of Engineering Mathematics* 34 (1998) 97109.
- 685 [21] R. Loubere, Validation test case suite for compressible hydrodynamics com-  
686 putation, Theoretical Division T-7 Los Alamos National Laboratory.
- 687 [22] D. L. Darmofal, K. Siu, A robust multigrid algorithm for the euler equations  
688 with local preconditioning and semi-coarsening, *Journal of Computational*  
689 *Physics* 151 (1999) 728756.

- 690 [23] P. Perrot, A to Z of Thermodynamics, Oxford University Press, 1998.
- 691 [24] O. LeMetayer, J. Massoni, R. Saurel, Elaborating equation of state for a  
692 liquid and its vapor for two-phase flow models, International Journal of  
693 Thermal Science 43 (2004) 265–276.
- 694 [25] S. LeMartelot, B. Nkonga, R. Saurel, Liquid and liquid-gas flows at all  
695 speeds: Reference solutions and numerical schemes., Research report 7935.
- 696 [26] R. A. DeVore, G. G. Lorentz, Constructive Approximation, Springer-  
697 Verlag, 1991.
- 698 [27] H. Guillard, C. Viozat, On the behaviour of upwind schemes in the low  
699 mach number limit, Comput. Fluids 105 (1993) 207–233.

700 **A. Derivation of the entropy residual as a function of the density, the**  
 701 **pressure and the speed of sound:**

702 The entropy residual is often expressed as a function of the entropy  $s(\vec{r}, t)$   
 703 as follows:

$$D_e(\vec{r}, t) = \partial_t s(\vec{r}, t) + \vec{u} \cdot \vec{\nabla} \cdot s(\vec{r}, t)$$

704 where all variables were defined previously. This form of the entropy residual is  
 705 not suitable for the low-Mach limit as explained in Section 2.1. It can be shown  
 706 that the entropy residual  $D_e(\vec{r}, t)$  can be recast as a function of the primitive  
 707 variables (pressure, velocity and density) and the speed of sound. This is the  
 708 objective of this appendix.

709 The first step is to use the chain rule, remembering that the entropy is assumed  
 710 function of the internal energy  $e$  and the density  $\rho$ :

$$D_e(\vec{r}, t) = s_e \frac{de}{dt} + s_\rho \frac{d\rho}{dt}$$

711 where  $s_x$  denotes the partial derivative of  $s$  with respect to the variable  $x$ . The  
 712 short-notation  $\frac{d}{dt}$  is used for the total or material derivative. We no need to  
 713 make the pressure appear: this can be achieved by noticing that the internal  
 714 energy is a function of the pressure and the density based on the definition of  
 715 the equation of state. Once again, by using the chain rule, it yields:

$$\begin{aligned} D_e(\vec{r}, t) &= s_e e_P \frac{dP}{dt} + (s_e e_\rho + s_\rho) \frac{d\rho}{dt} \\ &= s_e e_P \left( \frac{dP}{dt} + \frac{1}{s_e e_P} (s_e e_\rho + s_\rho) \frac{d\rho}{dt} \right) \\ &= s_e e_P \left( \frac{dP}{dt} + \left( \frac{e_\rho}{e_P} + \frac{s_\rho}{s_e e_P} \right) \frac{d\rho}{dt} \right) \end{aligned}$$

716 We are now close to the final result (see Eq. (8)). It remains to prove that the  
 717 term multiplying the material derivative of the density is equal to the speed  
 718 of sound square. The speed of sound is often defined as the partial derivative  
 719 of the pressure with respect to the density at constant entropy, which can be  
 720 recast as a function of the entropy as follows (see Appendix A.2 of [13]):

$$c^2 = \left( \frac{\partial P}{\partial \rho} \right)_s = P_\rho - \frac{s_\rho}{s_e} P_e = -\frac{e_\rho}{e_P} - \frac{s_\rho}{s_e e_P}$$

721 using the following relations (see Appendix A.1 of [13]):

$$P_e = \frac{1}{e_P} \text{ and } P_\rho = \frac{e_\rho}{e_P}$$

722 Then, the result follows.

723 **B. Derivation of the dissipative terms for the multi-D Euler equations**  
 724 **with variable area using the entropy minimum principle:**

725 The multi-D Euler equations with variable area are recalled here:

$$\begin{cases} \partial_t (\rho A) + \vec{\nabla} \cdot (\rho \vec{u} A) = 0 \\ \partial_t (\rho \vec{u} A) + \vec{\nabla} \cdot [A (\rho \vec{u} \otimes \vec{u} + P \mathbf{I})] = P \vec{\nabla} A \\ \partial_t (\rho E) + \vec{\nabla} \cdot [\vec{u} (\rho E + P)] = 0 \end{cases}$$

726 Assuming the existence of an entropy  $s$  function of the density  $\rho$  and the internal  
 727 energy  $e$ , the above system of equations admits the following entropy residual  
 728 [17]:

$$A \rho \left( \partial_t s + \vec{u} \cdot \vec{\nabla} \cdot s \right) \geq 0$$

729 when assuming  $P s_e + \rho^2 s_\rho = 0$ . An entropy function  $s$  verifying this equation  
 730 is also a solution of the second thermodynamic law for a reversible system,  
 731  $T ds = de - \frac{P}{\rho^2} d\rho$ , which implies  $s_e = T^{-1} \geq 0$ .

732 In order to apply the entropy viscosity method, dissipative terms are added to  
 733 each equation. Then, the entropy residual is derived again: extra terms due to  
 734 the dissipative terms will appear in the left-hand side. In order to prove the  
 735 minimum entropy principle, these extra terms are either recast as conservative  
 736 term, or shown to be positive.

737 The multi-D Euler equations with variable area with dissipative terms, yield:

$$\begin{cases} \partial_t (\rho A) + \vec{\nabla} \cdot (\rho \vec{u} A) = \vec{\nabla} \cdot f \\ \partial_t (\rho \vec{u} A) + \vec{\nabla} \cdot [A (\rho \vec{u} \otimes \vec{u} + P \mathbf{I})] = P \vec{\nabla} A + \vec{\nabla} \cdot g \\ \partial_t (\rho E) + \vec{\nabla} \cdot [\vec{u} (\rho E + P)] = \vec{\nabla} \cdot h \end{cases} \quad (32)$$

738 where  $f$ ,  $g$  and  $h$  are the dissipative terms to derive. Starting from the modified  
 739 system of equations given in Eq. (32), the entropy residual is derived again:

$$\begin{aligned} A \rho \left( \partial_t s + \vec{u} \cdot \vec{\nabla} \cdot s \right) &= s_e \left[ \vec{\nabla} \cdot h + g \vec{\nabla} u + \left( \frac{u^2}{2} - e \right) \vec{\nabla} \cdot f \right] \\ &+ \rho s_\rho \vec{\nabla} \cdot f \end{aligned} \quad (33)$$

740 The next step consists of choosing a definition for each of the dissipative terms  
 741 so that the left hand-side is proven positive. The right hand-side of Eq. (33)  
 742 can be simplified using the following relations,  $g = A \mu \vec{\nabla}^s \vec{u} + \vec{u} \otimes f$  and  $h =$   
 743  $\tilde{h} + \vec{u} \cdot g - 0.5 ||\vec{u}||^2 f$ , which yields:

$$A \rho \left( \partial_t s + \vec{u} \cdot \vec{\nabla} \cdot s \right) = s_e \left[ \vec{\nabla} \cdot \tilde{h} - e \vec{\nabla} \cdot f \right] + \rho s_\rho \vec{\nabla} \cdot f + A s_e \mu \vec{\nabla}^s \vec{u} \cdot \vec{\nabla} \vec{u}$$

744 The right hand-side is now integrated by part:

$$\begin{aligned} A \rho \left( \partial_t s + \vec{u} \cdot \vec{\nabla} \cdot s \right) &= \vec{\nabla} \cdot \left[ s_e \tilde{h} - s_e e f + \rho s_\rho f \right] - \\ &\vec{\nabla} \cdot \tilde{h} \vec{\nabla} s_e - f \vec{\nabla} (e s_e) - f \vec{\nabla} (\rho s_\rho) + A s_e \mu \vec{\nabla}^s \vec{u} \cdot \vec{\nabla} \vec{u} \end{aligned}$$



745 where  $\vec{\nabla}^s$  is the symmetric gradient. The term  $As_e\mu\vec{\nabla}\vec{u}^s\vec{\nabla}\vec{u}$  is positive and thus,  
 746 does not need any further modification. It remains to treat the other terms of  
 747 the right hand-side that we now call  $rhs$ :

$$rhs = \vec{\nabla} \cdot [s_e \tilde{h} - s_e e f + \rho s_\rho f] - \vec{\nabla} \cdot \tilde{h} \vec{\nabla} s_e - f \vec{\nabla} (e s_e) - f \vec{\nabla} (\rho s_\rho)$$

748 The first term of  $rhs$  is a conservative terms. By choosing carefully a definition  
 749 for  $\tilde{h}$  and  $f$ , the conservative term can be expressed as a function of the entropy  
 750  $s$ . It is also required to include the variable area in the choice of the dissipative  
 751 terms so that when assuming constant area, the regular multi-D Euler equations  
 752 are recovered. The following definitions for  $\tilde{h}$  and  $f$  are chosen:

$$\tilde{h} = A\kappa\vec{\nabla}(\rho e) \text{ and } f = A\kappa\vec{\nabla}\rho,$$

753 which yields, using the chain rule:

$$rhs = \vec{\nabla} \cdot (A\kappa\vec{\nabla}s) - A\kappa \underbrace{\left[ \vec{\nabla}(\rho e)\vec{\nabla}s_e + \vec{\nabla}\rho\vec{\nabla}(e s_e) + \vec{\nabla}(\rho s_\rho) \right]}_{\mathbf{Q}}$$

754 It remains to treat the term  $\mathbf{Q}$  that can be recast under a quadratic form,  
 755 following the work done in [13]:

$$\begin{aligned} \mathbf{Q} &= X^t \Sigma X \\ \text{with } X &= \begin{bmatrix} \vec{\nabla}\rho \\ \vec{\nabla}e \end{bmatrix} \text{ and } \Sigma = \begin{bmatrix} \partial_\rho(\rho^2 \partial_\rho s) & \partial_{\rho,e}s \\ \partial_{\rho,e}s & \partial_{e,e}s \end{bmatrix} \end{aligned}$$

756 The matrix  $\Sigma$  is symmetric and identical to the matrix obtained in [13]. The sign  
 757 of the quadratic form can be simply determined by studying the positiveness of  
 758 the matrix  $\Sigma$ . In this particular case, it is required to prove that the matrix is  
 759 negative definite: the quadratic form is in the right hand-side and is preceded of  
 760 a negative sign. According to [13], the convexity of the opposite of the entropy  
 761 function  $s$  with respect to the internal energy  $e$  and the specific volume  $1/\rho$  is  
 762 sufficient to ensure that the matrix  $\Sigma$  is negative definite.

763 Thus, the right hand-side of the entropy residual Eq. (33), are now either recast  
 764 as conservative terms, or known to be positive. Following the work done by [13],  
 765 the entropy minimum principle holds.